Secondary corrosion protection of FeCr(Al) model alloys at 600 °C – The influence of Cr and Al after breakaway corrosion

Corrosion Science 189 (2021) 109584

Contents lists available at ScienceDirect

Corrosion Science

journal homepage: www.elsevier.com/locate/corsci

Secondary corrosion protection of FeCr(Al) model alloys at 600 °C – The influence of Cr and Al after breakaway corrosion

J. Eklund *, A. Persdotter, I. Hanif, S. Bigdeli, T. Jonsson

Environmental Inorganic Chemistry, Department of Chemistry and Chemical Engineering, Chalmers University of Technology, S-412 96, Göteborg, Sweden

ARTICLE INFO

Keywords:
A. FeCrAl
A. Chromium
A. Aluminium
B. STEM
C. High temperature corrosion
C. Internal oxidation

ABSTRACT

The influence of Cr and Al content on the oxidation behaviour of FeCr(Al) model alloys after breakaway oxidation at 600 °C and the underlying mechanisms were investigated in detail with thermogravimetrical analysis (TGA), thermodynamic calculations and advanced electron microscopy. The results showed that a Cr-content of ≥18 wt% drastically reduced the growth rate of the Fe-rich oxide scale, formed after breakaway oxidation, for FeCrAl alloys but not for FeCr alloys. This was attributed to the ability of the Fe(18-25)CrAl alloys to prevent internal oxidation, which enables the formation of a healing layer.

1. Introduction

High temperature corrosion is an issue present in many applications, which often negatively impacts the efficiency of the involved processes and generally increases the maintenance costs due to accelerated material degradation. Chromia-forming stainless steels are often used in various corrosive environments to prevent rapid material degradation, attributed to the formation of a protective Cr-rich M_2O_3 oxide ($(Cr, Fe)_2O_3$). The material will display excellent corrosion protection at medium high temperatures, e.g. 600 °C, if the Cr-rich oxide scale remains intact. However, some high temperature applications generate corrosive species that result in a very corrosive environment, which can cause the protective oxide scale to break down. One example of such an application is biomass- and waste-fired boilers where the combustion release high levels of water vapour and alkali chlorides. In the presence of these compounds the $(Cr, Fe)_2O_3$ oxide scale may be depleted in Cr through two separate mechanisms: In the presence of alkali compounds, Cr depletion takes place due to the formation of alkali chromates [1–3]; In the presence of water vapour, Cr depletion is caused by evaporation of chromium oxy hydroxide ($CrO_2(OH)_2$) [4–7]. Both of these mechanisms eventually cause the protective $(Cr, Fe)_2O_3$ oxide to break down, which is followed by the formation of a faster growing multi-layered Fe-rich oxide scale. This phenomenon is generally referred to as breakaway oxidation. Previous research on breakaway oxidation of Fe-based alloys in a wide range of harsh conditions (at 600-650 °C) has shown that a similar type of Fe-rich oxide scale is formed, regardless of the environment [8–15].

A possible solution to prevent breakaway oxidation is to use alumina-forming alloys, i.e. FeAl or FeCrAl alloys, with the ability to form Al-rich M_2O_3 oxide scales at elevated temperatures. FeCrAl alloys are commonly used at higher temperatures than chromia-forming stainless steels since they are able to form an α-alumina scale above approximately 900 °C, which has a very high corrosion resistance [16–18]. However, at lower temperatures the α-alumina formation is very slow and the corrosion protection of the alloy may therefore depend on a transient alumina scale [19]. The transient alumina scale generally contains significant amounts of Fe and Cr which may negatively influence the resistance to alkali compounds and water vapour [20]. Accordingly, the protective oxide scale of commercial FeCrAl alloys has been shown to break down in the presence of alkali chlorides at 600 °C, which is followed by the formation of a fast growing Fe-rich oxide scale [21]. Pre-oxidation of FeCrAl alloys above 900 °C to pre-form an α-alumina has been shown to improve the corrosion resistance of the alloy by extending the time before the loss of the protective oxide scale in these harsh environments. However, due to the sensitivity to flaws and defects in these alumina scales, breakaway oxidation has been observed even for the pre-oxidized samples [22,23]. Thus, relying on the formation of a thin protective oxide scale which can withstand these harsh environments may not be a viable option. A different approach was recently investigated by Persdotter et al. [24] in which two different corrosion regimes were distinguished: Primary (Cr- and/or Al-rich M_2O_3 oxide scale(s)) and Secondary (multi-layered Fe-rich oxide scales)

* Corresponding author.
E-mail address: johekl@chalmers.se (J. Eklund).

https://doi.org/10.1016/j.corsci.2021.109584
Received 13 January 2021; Received in revised form 21 May 2021; Accepted 23 May 2021
Available online 26 May 2021

corrosion regimes. Contrary to the majority of the literature on high temperature corrosion that study focused on the secondary corrosion regime (i.e. the oxide scale formed after breakaway oxidation) and the possibility of improving the corrosion resistance of the Fe-rich oxide scale. The study showed that varying the amounts of Cr and Al in the FeCrAl alloys significantly influence the growth kinetics of the Fe-rich oxide scale. Increasing Cr content was shown to drastically reduce the growth rate of the Fe-rich oxide scale for FeCrAl alloys but not for FeCr alloys. This indicates a synergistic relationship between Cr and Al in the Fe-rich oxide scale. Increasing Al content was also shown to significantly reduce the growth rate of the Fe-rich oxide scale but only for FeCrAl alloys that exceeds a Cr content of 18 wt%. The mechanism(s) behind these observations are not fully understood but would be of great importance both from the perspective of material development as well as lifetime predictions for materials used in harsh environments.

The aim of this study is to increase the understanding of the influence of Cr and Al on the secondary corrosion protection of FeCr(Al) alloys (the Fe-rich oxide scale formed after breakaway oxidation). This was done by exposing FeCr(Al) model alloys, with varying Al and Cr content, in the presence of K_2CO_3 in order to rapidly break down the primary protection with limited influence on the secondary protection. K_2CO_3 has previously been reported to react with Cr-rich corundum type oxide to rapidly initiate breakaway oxidation [1,25–28]. The oxide scales formed in the secondary corrosion regime were analysed using Scanning Electron Microscopy (SEM) for general overview while specific features were analysed using Transmission Electron Microscopy (TEM). Energy dispersive X-ray spectroscopy was used for chemical analysis both in the SEM and TEM. In addition, the Calphad (CALculation of Phase Diagrams)-based software Thermo-Calc was used to calculate phase diagrams, relevant for the investigated alloys, aiding the interpretation of the microstructural analysis.

2. EXPERIMENTAL

2.1. Sample preparation

Three matrices of FeCr(Al) alloys with varying Cr and Al content were used in this study (compositions are shown in Table 1). The samples were cut into coupons with a dimension of 10 × 8 × 2 mm and a hole (1.5 mm in diameter) was drilled in the upper part of the coupons (for hanging the sample in the thermobalance). The samples were heat treated at 950 °C for one hour to achieve a more even grain size distribution (see Table 1) as well as to relax elongated grains in the bulk. Prior to exposure, the sample coupons were ground with SiC paper from P500 to P4000 and were finally polished down to 1 μm with diamond suspensions until a mirror-like surface was achieved.

2.2. Exposure

Prior to exposure, 1 mg/cm^2 K_2CO_3 was deposited onto the surface in order to break down the primary corrosion protection of the alloys in the initial stage of the exposures. The K_2CO_3 was deposited onto the samples by spraying a water solution saturated with K_2CO_3. A continuous flow of warm air was directed towards the sample during the spraying in order to evaporate the solution upon impact with the sample surface and to facilitate an even distribution of the salt. The deposited salt was weighed using a Sartorius^{TM} balance with microgram resolution. The samples were exposed isothermally in a Setaram Setsys Evolution TGA system in 5% O_2 + N_2 (bal.) at 600 °C for 48 hours. The total flow rate during the exposures was 1.5 cm/s (at 600 °C).

Table 1
Nominal composition and alloy grain sizes of model FeCr(Al) alloys used in this study.

Alloy name	Fe [wt%]	Cr [wt%]	Al [wt%]	Alloy grain size [μm]
Fe**2.25Cr**	Bal.	2.25	0	-
Fe**10Cr**	Bal.	10	0	-
Fe**18Cr**	Bal.	18	0	150
Fe**25Cr**	Bal.	25	0	-
Fe18Cr**0Al**	Bal.	18	0	150
Fe18Cr**1Al**	Bal.	18	1	280
Fe18Cr**3Al**	Bal.	18	3	400
Fe**5Cr**3Al	Bal.	5	3	500
Fe**10Cr**3Al	Bal.	10	3	650
Fe**18Cr**3Al	Bal.	18	3	400
Fe**25Cr**3Al	Bal.	25	3	350

2.3. Analysis and calculations

Cross sections of the exposed samples were prepared by first attaching thin silicon wafers onto the surfaces of the samples using glue. The glue was dried for about 24 hours before dry cutting the samples with a low speed diamond saw. The cross sections were milled using broad ion beam (BIB) milling with a Leica TIC 3X instrument to achieve a smooth surface for more accurate analysis. The three argon guns of the BIB instrument were operated at 8 kV for 6-10 hours.

The cross sections were analysed by means of SEM (imaged with backscattered electrons (BSE) mode) and energy dispersive X-ray spectroscopy (EDX) with an accelerating voltage of 10-20 kV using an FEI Quanta 200 equipped with an Oxford Instruments X-Max^N 80 T EDX detector. For images with higher spatial resolution a Leo ULTRA 55 FEG SEM was used (using ESB detector) with an accelerating voltage of 2 kV.

Transmission electron microscopy (TEM) was used to analyse the oxide scales in further detail. An FEI Titan 80-300 TEM equipped with an Oxford X-sight EDX detector for chemical analysis was used in this work. The microscope was operated both in conventional TEM mode as well as Scanning TEM (STEM) mode, at an accelerating voltage of 300 keV. High-Angle Annular Dark Field (HAADF) images were captured using the STEM imaging mode. The STEM/EDX quantification is reported in cationic percent (in at%) assuming stoichiometric oxides, due to large errors associated with oxygen quantification in EDX analysis. The quantification was performed in the TIA software using thickness correction with density 5-7 g/cm3 and an estimated lamella thickness (d) of 100-250 nm, chosen by chemical quantification in the known reference material of the investigated TEM lamella. Convergent beam electron diffraction (CBED) was performed on selected areas as a complement to the STEM analysis for phase determination.

The TEM lamellae were prepared by Focused ion beam (FIB) milling using an FEI Versa3D LoVac DualBeam, equipped with a Ga liquid metal ion source (LMIS), a Gas Injection System for pt deposition and an Omniprobe needle for lift-out of thin TEM lamellae. The instrument was operated in high vacuum mode at 30 keV, with varying beam currents (30 pA - 30 nA) throughout the lift-out procedure. The lift-out was performed from BIB-milled cross sections to facilitate the localization of a representative region as well as to minimize the difference in lamella thickness (wedge effect) throughout the oxide scale.

Isothermal (600 °C) binary phase diagrams (pO_2 vs cationic concentration (at%) Cr (Cr/(Cr + Fe + Al))) were produced using the Calphad-based software Thermo-Calc. The phase diagrams were calculated at different fixed Al-contents using the oxide database TCOX10. The phase diagrams were used in combination with the microstructural investigation to get a better understanding of the possible underlying mechanisms.

3. Results

3.1. Thermogravimetry

The oxidation properties of all included model alloys in dry oxygen (primary regime) have previously been investigated [24]. All alloys, except the low-alloyed Fe2.25Cr, formed thin slow-growing oxide scales indicating a primary protection. Exposure in the presence of K_2CO_3

resulted in rapid breakaway oxidation for all alloys, i.e transition from the primary to the secondary corrosion regime. The most representative kinetic behaviour for each alloy in the presence of K_2CO_3 is shown in Fig. 1. It is possible to distinguish two main groups of oxidation kinetics, i.e. fast and slow corrosion rates (and one intermediate, for Fe18Cr1Al). Thus, the different alloy compositions may provide poor or good secondary corrosion protection after breakaway oxidation. Despite of small differences in the behaviour within the different groups of alloys, the general interpretation of the oxidation kinetics will be considered similar within each group (fast- or slow-growing oxide scales) when discussing the mechanisms behind the observations.

The alloys displaying a poor secondary protection, i.e. Fe2.25Cr, Fe10Cr, Fe18Cr, Fe5Cr3Al and Fe10Cr3Al, showed very similar oxidation kinetics, resulting in a final mass gain within the range 5.5-5.9 mg/cm^2 after 48 hours of exposure. Two alloys (Fe10Cr and Fe18Cr) displayed an incubation time before breakaway (1 hour and 4 hours, respectively). However, these alloys have mass gains in the same range as the other alloys (that formed fast-growing oxide scales) suggesting that the relatively short incubation times did not significantly influence the final mass gain. All the alloys with poor secondary corrosion protection displayed rapid initial growth before transitioning into parabolic growth (except Fe18Cr) after about 2 hours with k_p values ranging from 0.5-0.9 mg^2 cm^{-4} h^{-1} (varied over time).

The alloys displaying a good secondary corrosion protection, i.e. Fe18Cr3Al and Fe25Cr3Al, showed similar oxidation kinetics and reached final mass gains ranging from 0.1-0.75 mg/cm^2 after 48 hours of exposure. However, the behaviour in the initial stages of the secondary corrosion regime differed for these two alloys. Fe18Cr3Al initially displayed a linear behaviour (for about an hour), while Fe25Cr3Al exhibited a logarithmic behaviour (for about 5 hours). Both alloys then transitioned into sub-parabolic behaviour. The order of parabolicity, i.e. the exponent in the relationship $m^{\alpha} \propto t$ ($\alpha = 2$ for parabolic growth), was higher for Fe25Cr3Al ($\alpha = 5$) than for Fe18Cr3Al ($\alpha = 3$).

Fe18Cr1Al displays an intermediate behaviour and may not be included in either of the groups mentioned above. Initially, it reached a relatively linear behaviour ($\alpha = 1.2$) which was maintained during the rest of the exposure. The slope is moderate and thereby has formed a significantly slower growing oxide scale (better secondary corrosion protection) than the alloys with poor secondary corrosion protection after 48 hours. However, no transition into sub-parabolic behaviour was observed during the 48 hours of exposure.

3.2. Microstructural investigation

The oxide scale microstructure was investigated by SEM/EDX on BIB milled cross sections and TEM/STEM/EDX on selected samples. All the alloys exposed in the presence of K_2CO_3 formed relatively homogeneously thick oxide scales after 48 hours exposure.

3.2.1. Fast-growing oxide scales

All the fast-growing (poorly protective) oxide scales displayed very similar microstructures, composed of outward-growing Fe-oxide and inward-growing mixed (Fe,Cr,Al) oxide, see e.g. Fig. 2a and [24]. The inward-growing oxide scale consists of alternating dark and bright regions (see Fig. 2a) which are suggested to be remnants from internal oxidation observed on the majority of the samples (exception: Fe2.25Cr). The chemical composition of the inward-growing scale varied for the different alloys while the oxide thicknesses (i.e. growth rate) and microstructure were similar. One of the alloys, Fe10Cr3Al, was chosen for detailed microstructural analysis, to represent the general oxide scale microstructure of the group of alloys exhibiting a poor secondary corrosion protection. The investigation of this oxide scale was then compared to the microstructure of the more protective oxide scales formed on the Fe18Cr3Al and Fe25Cr3Al alloys. Fig. 2a shows the oxide scale formed on Fe10Cr3Al after 48 h of exposure. The oxide scale was observed to be approximately 50 μm thick and consisted of an outward-growing Fe oxide scale (~30 μm) and an inward-growing mixed (Fe, Cr, Al) oxide scale (20 μm thick), resulting in an outward/inward ratio of 60/40. The outward growing oxide scale was bi-layered, interpreted to be comprised of an outer hematite (Fe_2O_3) layer (~3 μm) and an inner magnetite (Fe_3O_4) layer (~27 μm). The inward-growing oxide scale consisted of segments of darker contrast which reoccurred periodically throughout the scale. The frequency of alternations of bright and dark segments was gradually reduced when approaching the scale/metal interface. At the scale/metal interface, a zone of internal oxidation was observed. The microstructure suggests it to be internal oxidation. Bagas et al. [29] and Jonsson et al. [9] has

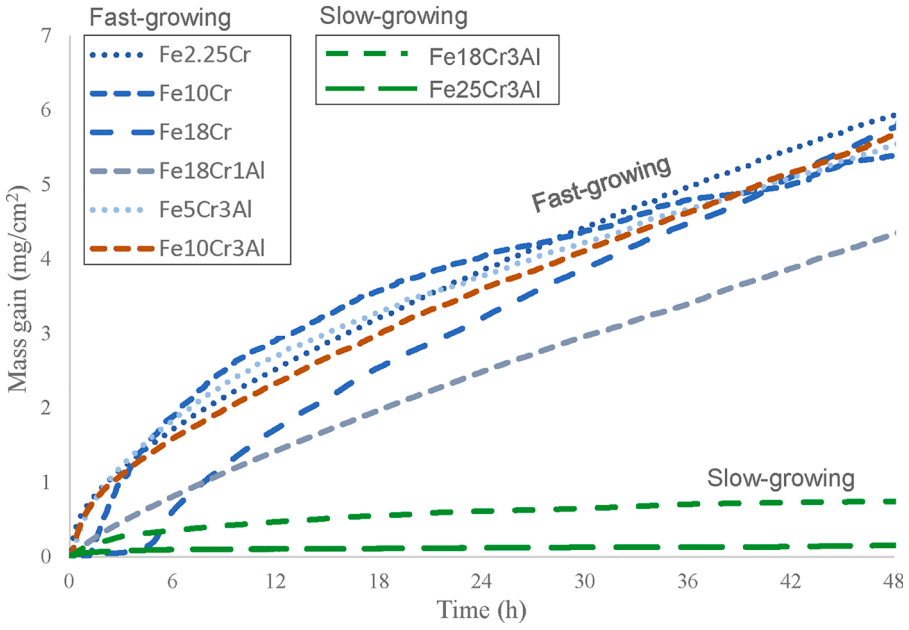

Fig. 1. Oxidation kinetics for FeCr(Al) model alloys during 48 hours isothermal exposures to 5% O_2 + N_2 (bal.) in the presence of K_2CO_3 at 600 °C (secondary corrosion regime). Two different types of behaviour can be distinguished, fast-growing and slow-growing oxide scales (and one intermediate (Fe18Cr1Al). The Fe10Cr3Al alloy is chosen to represent the fast-growing oxide scales.

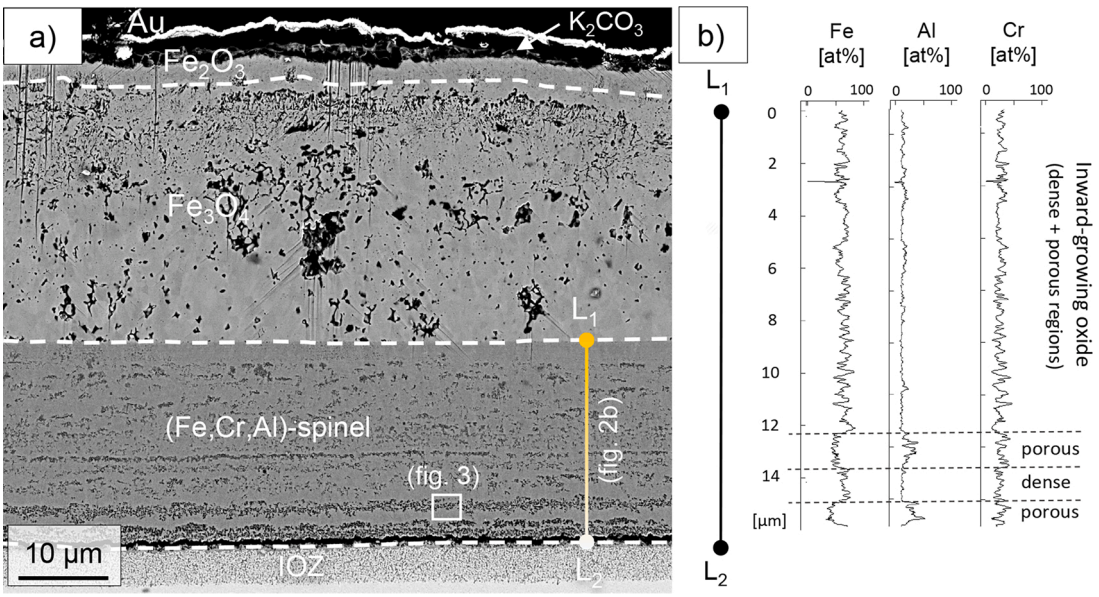

Fig. 2. a) SEM-BSE image of the oxide scale formed on Fe10Cr3Al after exposure to 5% O_2 + 75% N_2 in the presence of K_2CO_3 at 600 °C for 48 hours. b) STEM/EDX line scans of the inward-growing oxide (see marking L_1-L_2). Quantification is performed in the TIA software using thickness correction with parameters $\rho = 5$, d = 100 nm.

previously reported a miscibility gap in the Fe-Cr spinel at 600 °C. The equilibrium calculations in addition predicts that Cr-rich spinel precipitates form internal oxides surrounded by a Cr-depleted non-oxidized metal matrix. This was confirmed by STEM/EDX analysis across the zone, showing oxidized regions in a non-oxidized, highly Fe-enriched (90-100 at% Fe) metal matrix. This type of internal oxidation should be distinguished from the type of internal oxidation in which precipitates of chromia or alumina are segregated in a Cr/Al-depleted alloy matrix which tend to be stable at lower pO_2.

The inward-growing oxide was further investigated by STEM/EDX (see Fig. 2b). The lift-out position for the TEM lamella is indicated in Fig. 2a and the corresponding EDX line scan data (from L_1 to L_2) is

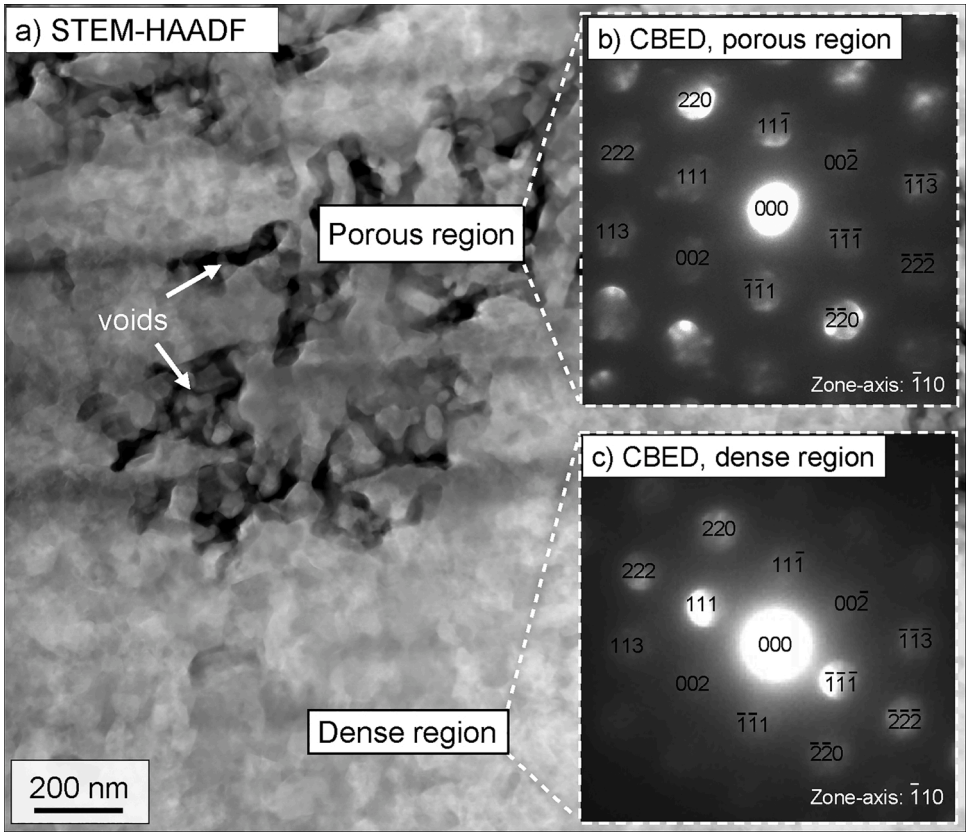

Fig. 3. a) STEM-HAADF image of part of the inward-growing oxide scale formed on Fe10Cr3Al after exposure to 5% O_2 + 75% N_2 in the presence of K_2CO_3 at 600 °C for 48 hours. b-c) CBED patterns (zone axis $\bar{1}10$) of the inward-growing oxide in the porous region (b) and dense region (c), indexed to be of spinel type.

shown in Fig. 2b. The STEM/EDX analysis showed that the porous region contained an average of 45 at% (40-50) Fe, 30 at% (15-50) Cr and 15 at % (15-35) Al, whereas the dense region contained an average of 65 at% (50-80) Fe, 22 at% (10-40) Cr and 14 at% (10-16) Al. Thus, the quantified Al content was considered homogeneous throughout the inward-growing scale in both type of regions, while the porous regions were slightly enriched in Cr and depleted in Fe. The Cr and Al contents in the dense region are in good agreement with the composition measured by SEM/EDX. However, it is to be noted that porosity makes the quantification difficult, especially for light elements such as Al. A thin-foil correction was used assuming a thickness of 100 nm, which may overestimate the amount of Al in the porous regions. Thus, it is probable that the Al concentration in the porous region is lower than what is measured in the STEM/EDX analysis.

Fig. 3a shows the difference in microstructure of the alternating dense and porous regions present in the inward-growing oxide scale in higher magnification. STEM/EDX analysis across the pores (not shown) also confirms the porosity by a significantly reduced X-ray count rate in the darker areas and only background noise detected in the black areas. The oxide grain size was measured to be in the range of 30-100 nm in both regions. Convergent beam electron diffraction (CBED) was used to determine the crystal structures of the dense and porous oxide regions. Fig. 3b-c shows CBED patterns from both regions, indexed as spinel oxides with the zone axis [$\bar{1}$10].

3.2.2. *Slow-growing oxide scales*

The microstructure of the slow-growing oxide scales (good secondary protection) formed on Fe18Cr3Al and Fe25Cr3Al were analysed in detail with SEM and TEM, see Figs. 4 and 5. The general microstructure was multi-layered, consisting of outward-growing Fe oxide and an inward-growing mixed (Fe, Cr and Al) oxide, i.e. similar to the alloys exhibiting a poor secondary corrosion protection. However, the oxide scale thicknesses on both of these alloys were drastically reduced in comparison to the alloys that formed fast-growing oxide scales.

The Fe18Cr3Al alloy exhibited a total oxide scale thickness of 3-4 μm, see Fig. 4a, with an outward-growing oxide scale of 2-2.5 μm and an inward-growing oxide scale of 1-1.5 μm, resulting in an outward/inward ratio of ~65/35. The outward-growing oxide scale was observed to be bi-layered, interpreted to consist of an outer hematite (Fe_2O_3) layer (300-400 nm) and an inner magnetite (Fe_3O_4) layer (~2 μm). The inward growing oxide scale consisted of an upper layer with darker contrast and a lower brighter layer in the SEM image (see Fig. 4a).

It was also observed that voids had formed close to the oxide/metal interface, see Figs. 4a and 5 b. The microstructure and chemical composition of the inward-growing oxide scale was investigated in detail by TEM (see Figs. 4 and 5). The lift-out position for the TEM lamella is indicated in Fig. 4a and the corresponding EDX line scan data (from L_1 to L_2) is shown in Fig. 4b. The chemical composition of the inward-growing oxide scale formed on Fe18Cr3Al (see Fig. 4b) is uniform and displayed a highly elevated Cr content of about 70 at% while its Al content was ranging from 15-25 at% (in average 15 at%). A depletion zone of Cr was also detected at the scale/metal interface to a depth of approximately 1 μm into the alloy. CBED confirmed the presence of spinel oxide in the inward-growing oxide scale, see indexed diffraction pattern in Fig. 5d. However, the large amounts of Cr + Al present in this oxide scale indicate a more complex microstructure, possibly consisting of several phases, and further detailed investigations are required to fully reveal the complex microstructure in this region.

The microstructural investigation of the inward-growing oxide scale (see Fig. 5a) suggests that the upper part is slightly more porous than the lower part. This would explain the darker contrast observed in the SEM. However, the investigation indicates that the oxide is affected throughout all of the inward-growing oxide scale, i.e. composed of elongated (20-100 nm) brighter regions, see Fig. 5c. It should also be noted that the TEM imaging showed indications of very small (5-15 nm) oxide grains or small domains in the inward-growing scale. However, in order to confirm this observation, further investigations are required.

The results from the SEM and TEM analysis of the Fe25Cr3Al alloy are shown in Figs. 6 and 7. The total oxide scale thickness was measured to be approximately 3.5 μm (see Fig. 6a) with an outward-growing oxide of about 2.5 μm and an inward-growing oxide of about 1 μm, resulting in an outward/inward ratio of ~70/30. In similarity to the Fe18Cr3Al alloy, voids were observed close to the scale/metal interface. It should be noted that a potassium- and Fe-rich phase was observed on top of the oxide scale. This is interpreted to be potassium ferrate from STEM/EDX-data, but not phase determination was performed for this phase.

The microstructure and chemical composition of the inward-growing oxide scale were investigated in detail by TEM/STEM/EDX (see Figs. 6 and 7). The lift-out position for the TEM lamella is marked in Fig. 6a and the results from the corresponding EDX line scan (from L_1 to L_2) is shown in Fig. 6b. The chemical composition of the inward-growing oxide scale is uniform displaying an elevated Cr content of about 70-80 at% and an

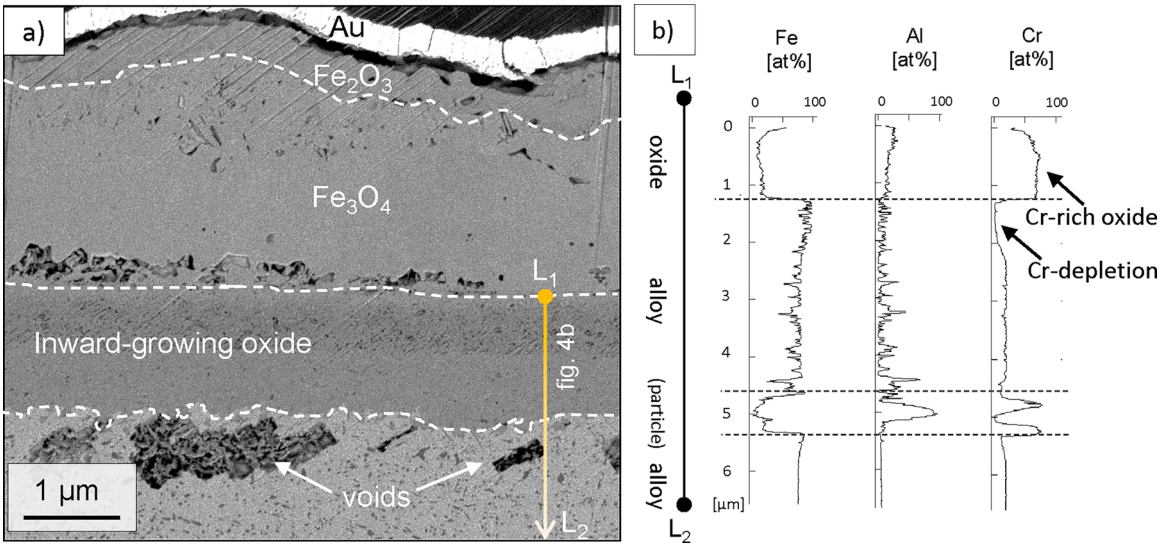

Fig. 4. a) SEM-BSE image of the oxide scale formed on Fe18Cr3Al after exposure to 5% O_2 + 75% N_2 in the presence of K_2CO_3 at 600 °C for 48 hours. b) STEM/EDX line scans of the inward-growing oxide scale and approximately 1 μm into the alloy (see marking L_1-L_2). Quantification is performed in the TIA software using thickness correction with parameters ρ = 7, d = 200 nm.

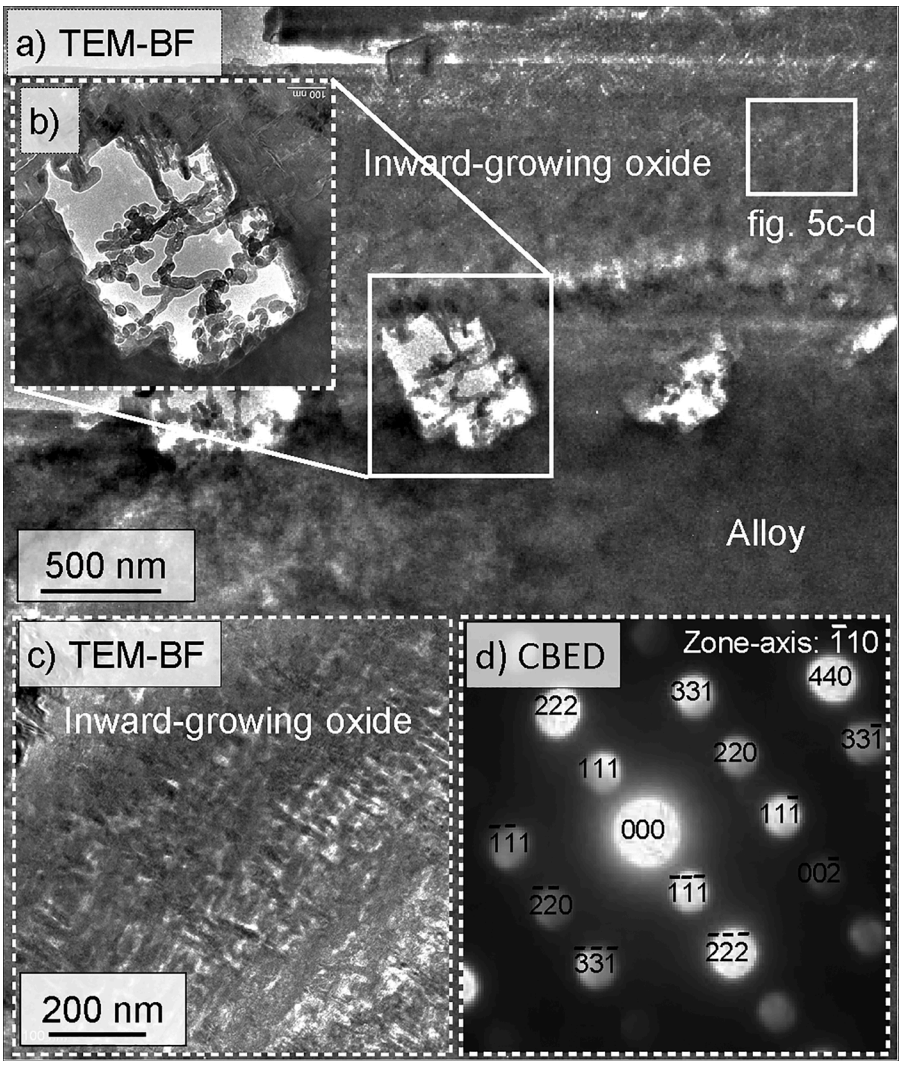

Fig. 5. a-c) TEM-BF images of the inward-growing oxide scale formed on Fe18Cr3Al after exposure to 5% O_2 + 75% N_2 in the presence of K_2CO_3 at 600 °C for 48 hours. d) CBED pattern (zone axis $\bar{1}10$) of the inward-growing oxide scale, indexed to be of spinel type.

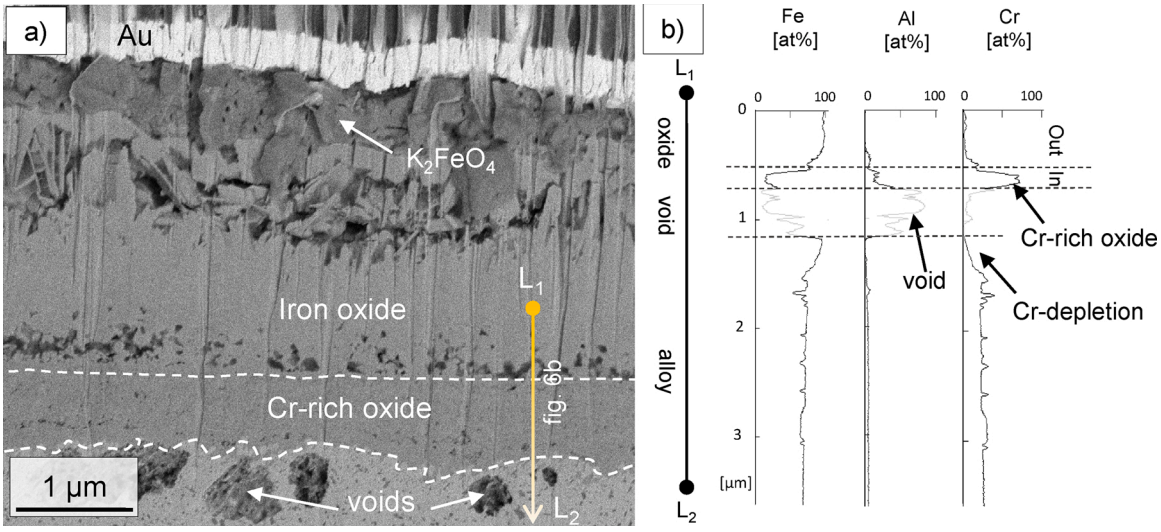

Fig. 6. a) SEM-BSE image of the oxide scale formed on Fe25Cr3Al after exposure to 5% O_2 + 75% N_2 in the presence of K_2CO_3 at 600 °C for 48 hours. b-c) TEM-HAADF image and STEM/EDX line scans of the inward-growing oxide scale and approximately 3 µm into the alloy (see marking L_1-L_2). Quantification is performed in the TIA software using thickness correction with parameters $\rho = 7$, $d = 250$ nm.

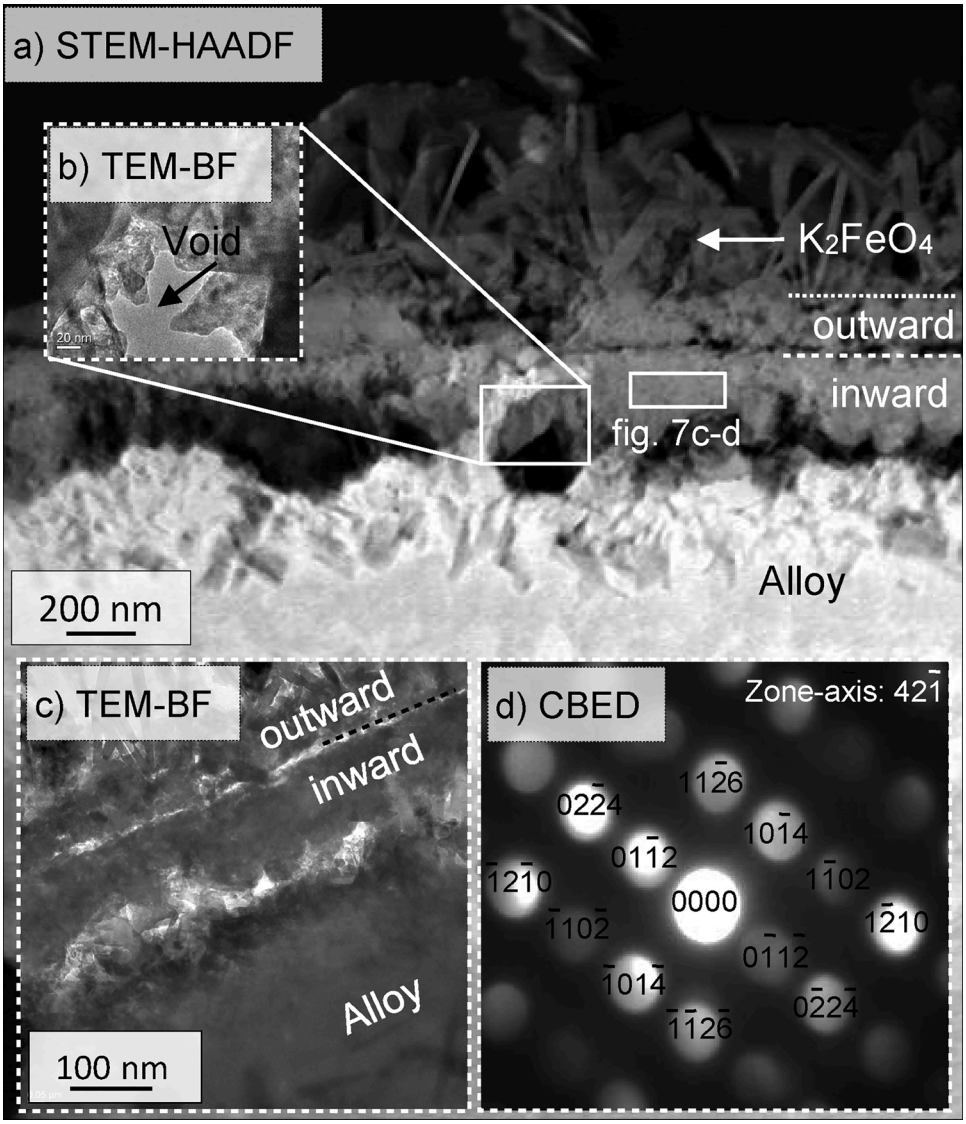

Fig. 7. a) STEM-HAADF image of the oxide scale formed on Fe25Cr3Al after exposure for to 5% O_2 + 75% N_2 in the presence of K_2CO_3 at 600 °C for 48 hours. b-c) TEM-BF images showing b) a void formed in the alloy near the M/O interface and c) the alloy and oxide layers. d) CBED pattern (zone axis 42$\bar{1}$) of the inward-growing oxide scale, indexed to be of corundum type.

Al content ranging from 10-20 at%, in similarity to the oxide formed on the Fe18Cr3Al. A depletion zone of Cr was also observed at the scale/metal interface on the Fe25Cr3Al alloy, approximately 0.5-1 μm deep into the alloy (see Fig. 6b). The TEM diffraction (CBED) shows the presence of Cr-rich corundum type oxide in the inward-growing oxide. However, as for the Fe18Cr3Al, it is possible that there are local phase variations, due to the small size of the analysed volume using CBED, as well as the challenge experienced when obtaining diffraction patterns from many different regions. It should also be noted that the microstructural investigation showed indications of very small oxide grains or small domains of approximately 5-15 nm, similar to the inward-growing oxide scale formed on Fe18Cr3Al. However, this observation needs further investigation to be confirmed.

3.3. Thermodynamic calculations

Isothermal phase diagrams were calculated at different fixed concentrations of Al (0 at%, 6 at% and 15 at%) to facilitate the interpretation of the complex oxide scale microstructure, see Fig. 8. The fixed concentrations of Al were chosen to aid the interpretation of the FeCrAl-O system when increasing the amount of Al. Note that the Al concentrations are including oxygen in phase regions including oxides and should not be considered the cationic concentration of Al. The selected Al concentrations can therefore not be directly correlated to the detected amount in the inward-growing oxides scales formed on the investigated FeCr1Al (5-6 at% Al) and FeCr3Al (15 at%) model alloys. However, the changes in the phase diagrams upon the addition of Al give valuable information about differences in driving forces for FeCr and FeCrAl alloys. The equilibrium calculations can also give insights into what phases are stable after the rapid initial oxidation. This work focuses on the corrosion front, i.e. where pO_2 is relatively low (10^{-30} -10^{-15} atm). In the absence of Al (see Fig. 8a-b), four different phase regions can be distinguished at pO_2 in the range of 10^{-25} - 10^{-15} atm, namely S_{Fe}, (S_{Fe}+ S_{Cr}), S_{Cr} and (S_{Cr}+C_{Cr}). S_{Fe} and S_{Cr} represents Fe-rich and Cr-rich spinel respectively and C_{Cr} represents a Cr-rich corundum type oxide. Note that the subscripts are used to simplify the interpretation of the phase diagram and that the composition of phases with the same subscript may vary between different phase regions. Fig. 8a shows the binary FeCr phase diagram with the three first phase regions (S_{Fe}, (S_{Fe}+ S_{Cr}), S_{Cr}) being stable at 0-67 cationic% Cr while the fourth phase region (S_{Cr}+C_{Cr}) is stable at 67-100 cationic% Cr. At a lower pO_2 (10^{-30} - 10^{-25} atm) the thermodynamic calculations predict the phase region

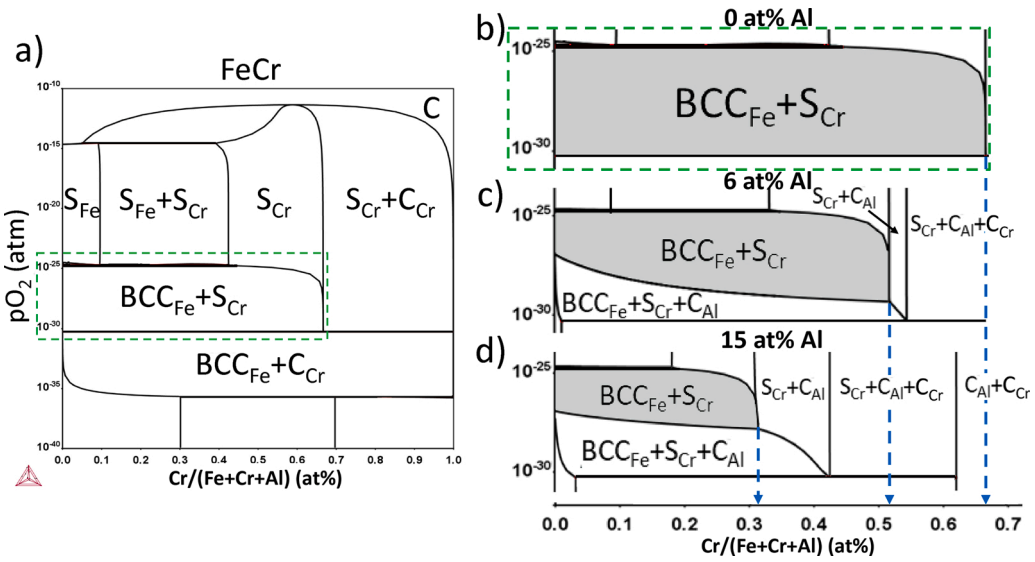

Fig. 8. Phase diagrams for the FeCr(Al) system at 600 °C calculated with Thermo-Calc. b) is a magnified FeCr diagram indicated by the dashed rectangle in a). c) and d) corresponds to the phase diagrams at fixed Al concentrations of 6 and 15 at%, respectively. The vertical dashed lines in b), c) and d) indicate the maximum Cr-content at which the two-phase region, $BCC_{Fe}+S_{Cr}$, is stable.

($BCC_{Fe}+S_{Cr}$) to be stable at 0-67 cationic% Cr while ($S_{Cr}+C_{Cr}$) is stable at 67-100 cationic% Cr. The phase region ($BCC_{Fe}+S_{Cr}$) represents the internal oxidation zone in which Cr-rich spinel precipitates are dispersed in a Cr-depleted alloy matrix.

The region marked by the green rectangle in Fig. 8a is plotted for the fixed Al-contents 0, 6 and 15 at% in Fig. 8b-d. The grey regions indicate the internal oxidation zone ($BCC_{Fe}+S_{Cr}$). The thermodynamic calculations indicate that increasing the Al concentration in the FeCr-O system divides the internal oxidation zone ($BCC_{Fe}+S_{Cr}$) into two different types of internal oxidation zones, i.e. the two-phase type ($BCC_{Fe}+S_{Cr}$) and a three-phase type ($BCC_{Fe}+S_{Cr}+C_{Al}$). In addition, the ($S_{Cr}+C_{Cr}$) region is divided into the two and three-phase regions ($S_{Cr}+C_{Al}$) and ($S_{Cr}+C_{Al}+C_{Cr}$). The stability range (Cr concentration) for the internal oxidation zone ($BCC_{Fe}+S_{Cr}$) is reduced with increasing Al concentration (the highest Cr concentration at which it is stable is indicated by the blue dashed lines in Fig. 8b-d). The internal oxidation zone is stable at up to 67 cationic% Cr with 0 at% Al while it is only stable at up to 32 cationic% Cr when the system contains 15 at% Al. Simultaneously, the Cr concentration at which a transition into a two or three-phase region where spinel oxide is in equilibrium with a Cr-rich corundum type oxide is reduced with increasing Al-content.

4. Discussion

Breakaway oxidation is a widely known phenomenon within the high temperature corrosion field. This often results in high material degradation and is in some cases considered the end of the lifetime of a material. While the majority of literature is focusing on understanding/preventing breakaway oxidation to improve the primary protection of the alloys, this paper is focused on understanding the influence of alloying elements on the corrosion behaviour of FeCr(Al) alloys in the secondary corrosion regime, i.e. after breakaway oxidation. The oxide scale microstructure of Fe-based alloys after breakaway oxidation at medium high temperatures (about 600 °C) has in many cases been shown to consist of a fast-growing Fe-rich multi-layered oxide scale [16,30]. This scale can typically be divided into an outward-growing Fe-oxide and an inward-growing spinel [8–15]. Persdotter et al. [24] recently showed that the growth rate of this type of oxide scale could be significantly reduced upon addition of combinations of Cr, Al and Ni.

The thermogravimetrical analysis (TGA) of the FeCr(Al) alloys included in this study clearly shows a rapid transition into breakaway oxidation and the secondary corrosion regime, see Fig. 1. In addition, the oxidation kinetics shows that the alloys exhibit two different kinetics within the secondary regime. All FeCr alloys (Cr-content of 2.25-18 wt %) and FeCrAl alloys with <18 wt% Cr and <3 wt% Al display similar oxidation kinetics, i.e. approximately parabolic behaviour with corrosion rates in the range of oxidation of pure Fe/low-alloyed steels in dry O_2 [8,31]. However, the FeCrAl alloys with ≥ 18 wt% Cr and 3 wt% Al displays significantly reduced growth rates, transitioning into a sub-parabolic behaviour at an early stage of the oxidation process. Even though the alloys display large differences within the secondary corrosion regime all alloys have formed a similar type of Fe-rich multi-layered oxide scale, see Figs. 2,4 and 6. This type of oxide scale microstructure, consisting of outward-growing Fe-oxide and inward-growing Fe, Cr, (Al)-oxide, is in agreement with previous observations [8–15]. The microstructure has been explained by different diffusivities of the alloying elements in the spinel phase [32]. Apart from the oxide scale thickness (i.e. growth rate), the microstructural investigation reveals two important microstructural differences between the fast-growing and the slow-growing oxide scales. Firstly, the alloys forming slow-growing oxide scales display higher Cr-enrichment in the lower part of the inward-growing oxide scale and a Cr-depletion zone underneath the oxide. Secondly, the alloys forming fast-growing oxide scales (except Fe2.25Cr) have an inward-growing scale consisting of alternating porous and dense bands and have in addition suffered from internal oxidation in which Cr-rich spinel precipitates are surrounded by Cr-depleted metal as predicted by the equilibrium calculations (see Fig. 8) [11].

4.1. The formation of a healing layer

The concentrations of Cr and Al are observed to be higher in the inward-growing oxide scale than in the alloy for all the investigated model alloys. This is attributed to the rapid outward diffusion of Fe (compared to Cr and Al) from the inward-growing scale [32]. However, the inward-growing part of the slow-growing oxide scales showed significantly higher levels of Cr than the fast-growing oxide scales and 0.5-1 μm deep depletion zones (Cr) can be observed in the metal underneath the slow-growing oxide scales (see Figs. 4 and 6). The depletion zones imply that the alloy below the corrosion front have supplied the Cr-rich scales with Cr. Using diffusivity data from binary Fe–Cr alloys [33], measured at higher temperatures and extrapolated to 600 °C

by Young et al. [34] (D_{Cr} of $10^{-14.5}$ cm^2 s^{-1}), a depletion zone of about 40 nm could be expected after 1 hour of exposure at 600 °C. Jonsson et al. [9] experimentally found that the depletion zone for an Fe10Cr model alloy was about 80 nm after 1 hour of exposure at 600 °C, i.e. slightly higher than the estimated value. Nevertheless, the much deeper depletion zones (0.5-1 μm) found in the present study indicates that the depletion started at an early stage of the exposure and not during the final hours. The TGA data shows that the slow-growing sub-parabolic kinetics started already after about 1-4 hours. Thus, the high Cr-enrichment may be connected to the early transition into sub-parabolic protective behaviour and the continuous supply of Cr from the alloy to the oxide scale. It may be noted that no depletion zones of Al were observed beneath the protective secondary scales. The Al seems to play a more passive role in the secondary protection.

Previous research often attributes these types of kinetic transitions to the formation of a healing layer [12,13,35–38]. For chromia-forming steels, Cr-enrichment close to the oxide/metal interface is generally interpreted as the formation of a Cr-rich corundum type $(Fe_x, Cr_{1-x})_2O_3$ healing layer. After 48 hours of exposure, both Fe18Cr3Al and Fe25Cr3Al display compositions in the inward-growing oxide scale (more than 70 cationic% Al + Cr), which would suggest that they are of corundum type, and not of spinel type. This is because the structure of the spinel oxide ($(M^{2+}M_2^{3+})O_4$), in which the divalent ions mainly occupy the tetrahedral sites and the trivalent ions mainly occupy the octahedral sites, limits the maximum amount of di- and trivalent ions (max 33.3 at % divalent and 67.7 at% trivalent). The oxidation state of Fe is known to be either divalent or trivalent while Cr and Al are more restricted to be trivalent [39]. Additionally, even though Cr is able to be divalent, Liang et al. experimentally investigated the valency and site position in magnetite with incorporation of varying amounts of Cr [40]. Their study strongly indicated that Cr was present in the trivalent state and positioned mainly in the octahedral sites. Thus, the fact that the cationic concentration of Cr + Al exceeds 67 cat% in the inward-growing oxide scale for both alloys indicate the presence of a corundum type oxide. However, the thickness of the Cr-rich layers observed on Fe18Cr3Al and Fe25Cr3Al in this study does not follow a predicted thickness of a diffusion-controlled growth of a Cr-rich corundum phase such as Cr_2O_3 as reported e.g. by Hallström et al. [41]. In addition, the diffraction pattern in Fig. 5d strongly suggests the presence of spinel in the inward-growing oxide scale formed on the Fe18Cr3Al alloy. Thus, the high amounts of Cr and Al (Cr + Al = 80 at%>>67.7 at%) observed in the inward-growing oxide scale of Fe18Cr3Al suggests either of the following:

a) There are local phase variations in the inward-growing scale that are not distinguished by the TEM analysis in this study.
b) That the oxide scale has a spinel type crystal structure in which Cr^{3+} ions occupy tetrahedral sites or have been reduced to Cr^{2+} ions.

The diffraction pattern shown in Fig. 7c suggests that the inward-growing oxide scale of Fe25CrAl has a corundum structure. This possibly indicates that the Cr-rich spinel observed on the Fe18Cr3Al may be meta-stable under the exposure conditions in the present study and that a phase transformation may occur after longer exposure times. A similar phase transformation, from a Cr-rich spinel to a corundum type oxide was observed by Col et al. with Raman-mapping on a 304 L sample after oxidation in dry O_2 at 850 °C for 312 hours [38]. The suggested phase transformation is in agreement with the thermodynamic calculations (see Fig. 8c-d) showing that the highly Cr-enriched inward--growing scale of both Fe18Cr3Al and Fe25Cr3Al (which seemingly have not suffered from internal oxidation) should be within the two- or three-phase regions (S_{Cr}+C_{Al}+C_{Cr} and C_{Al}+C_{Cr}) in which spinel is in equilibrium with corundum. Accordingly, the inward-growing oxide scale of Fe25Cr3Al is expected to more rapidly transform into a corundum-type oxide due to a higher Cr-content. Thus, a higher Cr content facilitates the formation of a healing layer.

4.2. The role of the internal oxidation

The formation of an internal oxidation zone, as observed at the scale/metal interface below the fast-growing oxide scales (see Fig. 2a), may be explained by the thermodynamic calculations. The FeCr phase diagram shows that the two-phase region BCC_{Fe}+S_{Cr} (corresponding to a specific type of internal oxidation zone) is stable below the spinel, see Fig. 8. The absence of an internal oxidation zone for Fe2.25Cr may be explained by the low Cr-content giving very slow kinetics to form Cr-rich spinel precipitates (see Fig. 8a). In addition, the alloys suffering from internal oxidation exhibit a specific microstructural feature in the inward-growing spinel, i.e. dense and porous bands/regions that alternate in a periodic manner and with a reducing frequency closer to the metal/oxide interface. The banded structure is believed to be remnants from the internal oxidation zone. Jonsson et al. [9] suggested that the Fe-rich metal left in the internal oxidation zone rapidly oxidize, leaving pores behind, which is in good agreement with the porous bands observed in this study. The periodicity of the banded structure has not been previously explained and is not fully understood. However, considering that the porous bands may enable faster transport of oxygen through the oxide scale, the underlying metal could be exposed to new conditions, i.e. a higher oxygen partial pressure. Assuming a higher pO2, outside the stability region for the internal oxidation (of type BCC_{Fe}+S_{Cr}), this would result in the formation of a dense spinel oxide (e.g. S_{Cr}), explaining the dense bands in the inward-growing scale. If a dense spinel is formed, the oxygen partial pressure would again be reduced, resulting in internal oxidation if crossing the threshold of the stability region for the two-phase region BCC_{Fe}+S_{Cr}. As the total oxide thickness increases, each cycle is expected to take longer time which would result in thicker periodic bands closer to the metal/oxide interface. This is in good agreement with the experimental results in this study, see Figs. 2 and 8a. Thus, assuming that this process would continue, the internal oxidation would result in a continued loop of rapid oxidation of mainly Fe (Fe-rich metal in the internal oxidation zone), which would also explain why all alloys that have exhibits internal oxidation display similar oxidation kinetics as low-alloyed steels. Thus, the key behind the protective or non-protective behaviour in the secondary corrosion regime may be whether or not an alloy suffers from internal oxidation.

4.3. The synergistic effects of Cr and Al

The influence of Cr and Al on the transition from fast- to slow-growing oxide scales in this study is apparent. However, the underlying mechanism has proven to be rather complex. At first glance, the influence of Cr seems to differ between the FeCr and FeCrAl systems. This is illustrated by comparing Fe10Cr(3Al) and Fe18Cr(3Al), where the FeCr system displays no effect of Cr content, whereas the FeCrAl system transitioned from fast- to slow-growing behaviour. The mechanism behind this effect may be enlightened by the phase diagrams in Fig. 8. The diagrams reveal several important differences upon adding Al to the FeCrO system. Firstly, the internal oxidation zone (BCC_{Fe}+S_{Cr}) is stable at higher Cr-content for FeCr alloys than for FeCrAl alloys, i.e. less Cr is needed in order to move out of the internal oxidation mode. This region is in addition continuously shifted to the left in the phase diagram with increasing Al concentration, i.e. towards a lower Cr-content. Secondly, the transition into the phase regions at which a spinel is in equilibrium with corundum type oxide occurs at a lower Cr-content with higher Al concentration. Thus, the influence of Al observed in FeCrAl alloys exposed in corrosive environments (secondary corrosion regime) is suggested to primarily be the reduced concentration of Cr necessary to prevent internal oxidation. SEM-EDX and STEM-EDX showed that all alloys containing 3 wt% Al (Fe5Cr3Al, Fe10Cr3Al, Fe18Cr3Al and Fe25Cr3Al) display roughly 15 cationic% Al in the inward-growing oxide scale. The phase diagrams (see Fig. 8d) indicate that when the

system contains 15 at% Al the internal oxidation zone ($BCC_{Fe}+S_{Cr}$) is stable up to about 32 cationic% Cr (while the three-phase type of internal oxidation, $BCC_{Fe}+S_{Cr}+C_{Al}$, is stable up to 43 cationic% Cr, but at a lower pO_2). This is in contrast to the FeCr system (see Fig. 8a) in which the internal oxidation zone is stable at up to 67 cationic% Cr. Persdotter et al. [24] showed that the Fe18Cr alloy display a Cr content of about 43 cationic% in the inward-growing spinel after 48 hours of exposure in dry O_2 in the presence of K_2CO_3. Thus, it would still be within the stability range of the internal oxidation zone. Both Fe18Cr and Fe18Cr1Al display similar Cr-content in the inward-growing spinel indicating that the same may apply for Fe18Cr3Al alloy at an early stage of the oxidation process. However, with a higher Al content the phase diagram indicates that the Fe18Cr3Al alloy may be outside of the stability range of internal oxidation at this Cr content. This is in agreement with the microstructural analysis, which shows that none of the alloys forming slow-growing oxides within the secondary corrosion regime (Fe18Cr3Al and Fe25Cr3Al) display neither formation of an internal oxidation zone nor periodic bands of dense and porous oxide. Note that the phase diagrams should not be considered exact predictions of the phases formed during the relatively short exposures (not in equilibrium) but rather indications of the involved driving forces and directions towards which the oxidation process may proceed.

4.4. Summary

The microstructural analysis and thermodynamic calculations suggest that the two different oxidation kinetics within the secondary corrosion regime may be explained by the ability of an alloy to rapidly form a protective spinel and/or a corundum type healing layer at the metal/oxide interface. One of the most important criteria for the formation of a healing layer is that it has to form faster than the Fe-rich oxide scale grows. Alloys that form an internal oxidation zone do not fulfil this condition since the internal oxidation results in rapid oxidation. Thus, the ability of an alloy to form a healing layer after transitioning into the secondary corrosion regime may rely on its ability to prevent internal oxidation from occurring. This is facilitated for alloys with high Cr content and increasingly so upon increasing the concentration of Al in the system due to a reduced range of Cr content at which the internal oxidation zone is stable.

5. Conclusions

All FeCr(Al) alloys included in this study clearly show a rapid transition into breakaway oxidation and the secondary corrosion regime. Two different oxidation behaviours were observed within the secondary corrosion regime: the formation of fast- or slow-growing oxide scales. The fast-growing oxide scales that formed in the secondary corrosion regime are suggested to be a result of a continuous loop of rapid internal oxidation, resulting in a porous inward-growing oxide scale with oxidation kinetics in the same range as oxidation of iron. The protective behaviour of the slow-growing oxide scales may be explained by the ability of an alloy to prevent internal oxidation, thereby enabling the formation of a corundum-type healing layer. The microstructural investigation and the thermodynamic calculations suggest that an increasing Cr content enables the alloy to prevent internal oxidation, whereas the influence of Al is suggested to be primarily to shift the range of the stability region of internal oxidation, reducing the Cr-content necessary to inhibit the formation of an internal oxidation zone.

Data Availability

The raw/processed data required to reproduce these findings cannot be shared at this time due to technical or time limitations.

CRediT authorship contribution statement

Johan Eklund: Conceptualization, Methodology, Validation, Investigation, Data curation, Writing - original draft, Writing - review & editing, Visualization.

Amanda Persdotter: Conceptualization, Investigation, Validation, Data curation, Writing - review & editing.

Imran Hanif: Investigation, Writing - review & editing.

Sedigheh Bigdeli: Software, Investigation, Writing - review & editing.

Torbjörn Jonsson: Conceptualization, Writing - review & editing, Supervision, Project administration, Funding acquisition.

Declaration of Competing Interest

The authors declare that they have no known competing financial interests or personal relationships that could have appeared to influence the work reported in this paper.

Acknowledgements

This work was carried out within the High Temperature Corrosion Centre (HTC) at Chalmers University of Technology and with support from VINNOVA, Sweden's Innovation Agency, within the Metallic Materials programme, that are hereby gratefully acknowledged together with the Swedish Energy Agency and the member companies (AB Sandvik Materials Technology, Kanthal AB, Energiforsk AB, MH Engineering AB, Thermo-Cale Software AB, Valmet Technologies Oy, Sumitumo SHI FW Energia Oy, Babcock and Wilcox Volund A/S and MEC BioHeat and Power A/S). The research was performed in part at the Chalmers Materials Analysis Laboratory, CMAL.

References

[1] J. Pettersson, N. Folkeson, L.-G. Johansson, J.-E. Svensson, The Effects of KCl, K2SO4 and K2CO3 on the High Temperature Corrosion of a 304-Type Austenitic Stainless Steel, Oxidation of Metals 76 (2011) 93–109.
[2] J. Pettersson, H. Asteman, J.E. Svensson, L.G. Johansson, KCl Induced Corrosion of a 304-type Austenitic Stainless Steel at 600°C; The Role of Potassium, Oxidation of Metals 64 (2005) 23–41.
[3] S. Karlsson, J. Pettersson, L.-G. Johansson, J.-E. Svensson, Alkali Induced High Temperature Corrosion of Stainless Steel: The Influence of NaCl, KCl and CaCl2, Oxidation of Metals 78 (2012) 83–102.
[4] H. Asteman, K. Segerdahl, J.E. Svensson, L.G. Johansson, M. Halvarsson, J.E. Tang, p. trans tech, Oxidation of stainless steel in H2O/O-2 environments - Role of chromium evaporation, in: P. Steinmetz, I.G. Wright, G. Meier, A. Galerie, B. Pieraggi, R. Podor (Eds.), High Temperature Corrosion and Protection of Materials 6, Prt 1 and 2, Proceedings, Trans Tech Publications Ltd, Zurich-Uetikon, 2004, pp. 775–782.
[5] H. Asteman, J.-E. Svensson, M. Norell, L.-G. Johansson, Influence of Water Vapor and Flow Rate on the High-Temperature Oxidation of 304L; Effect of Chromium Oxide Hydroxide Evaporation, Oxidation of Metals 54 (2000) 11–26.
[6] H. Asteman, J.E. Svensson, L.G. Johansson, M. Norell, Indication of Chromium Oxide Hydroxide Evaporation During Oxidation of 304L at 873 K in the Presence of 10% Water Vapor, Oxid Met 52 (1999) 95–111.
[7] H. Asteman, J.E. Svensson, L.G. Johansson, Evidence for Chromium Evaporation Influencing the Oxidation of 304L: The Effect of Temperature and Flow Rate, Oxidation of Metals 57 (2002) 193–216.
[8] B. Pujilaksono, T. Jonsson, H. Heidari, M. Halvarsson, J.E. Svensson, L. G. Johansson, Oxidation of Binary FeCr Alloys (Fe–2.25Cr, Fe–10Cr, Fe–18Cr and Fe–25Cr) in O2 and in O2 + H2O Environment at 600 °C, Oxidation of Metals 75 (2011) 183–207.
[9] T. Jonsson, B. Pujilaksono, H. Heidari, F. Liu, J.E. Svensson, M. Halvarsson, L. G. Johansson, Oxidation of Fe–10Cr in O2 and in O2+H2O environment at 600°C: A microstructural investigation, Corrosion Science 75 (2013) 326–336.
[10] T. Jonsson, H. Larsson, S. Karlsson, H. Hooshyar, M. Sattari, J. Liske, J.E. Svensson, L.G. Johansson, High-Temperature Oxidation of FeCr(Ni) Alloys: The Behaviour After Breakaway, Oxidation of Metals 87 (2017) 333–341.
[11] T. Jonsson, S. Karlsson, H. Hooshyar, M. Sattari, J. Liske, J.E. Svensson, L. G. Johansson, Oxidation After Breakdown of the Chromium-Rich Scale on Stainless Steels at High Temperature: Internal Oxidation, Oxid Met 85 (2016) 509–536.
[12] T. Gheno, D. Monceau, D.J. Young, Mechanism of breakaway oxidation of Fe–Cr and Fe–Cr–Ni alloys in dry and wet carbon dioxide, Corrosion Science 64 (2012) 222–233.

[13] T. Gheno, D. Monceau, D.J. Young, Kinetics of breakaway oxidation of Fe–Cr and Fe–Cr–Ni alloys in dry and wet carbon dioxide, Corrosion Science 77 (2013) 246–256.
[14] A.N. Hansson, M. Montgomery, M.A.J. Somers, Development of the inner oxide zone upon steam oxidation of an austenitic stainless steel, Materials at High Temperatures 26 (2009) 39–44.
[15] N. Otsuka, Y. Shida, H.J.O.o.M. Fujikawa, Internal-external transition for the oxidation of Fe-Cr-Ni austenitic stainless steels in steam, Oxidation of Metals 32 (1989) 13–45.
[16] P. Kofstad, High temperature corrosion, Elsevier applied science, London; New York, N.Y, 1988.
[17] H. Götlind, F. Liu, J.E. Svensson, M. Halvarsson, L.G. Johansson, The Effect of Water Vapor on the Initial Stages of Oxidation of the FeCrAl Alloy Kanthal AF at 900 °C, Oxidation of Metals 67 (2007) 251–266.
[18] F. Liu, H. Josefsson, J.-E. Svensson, L.-G. Johansson, M. Halvarsson, TEM investigation of the oxide scales formed on a FeCrAlRE alloy (Kanthal AF) at 900°C in dry O2 and O2 with 40% H2O, Materials at High Temperatures 22 (2005) 521–526.
[19] N. Israelsson, K.A. Unocic, K. Hellström, T. Jonsson, M. Norell, J.-E. Svensson, L.-G. Johansson, A Microstructural and Kinetic Investigation of the KCl-Induced Corrosion of an FeCrAl Alloy at 600 °C, Oxidation of Metals 84 (2015) 105–127.
[20] H. Josefsson, F. Liu, J.E. Svensson, M. Halvarsson, L.G. Johansson, Oxidation of FeCrAl alloys at 500–900°C in dry O2, Materials and Corrosion 56 (2005) 801–805.
[21] N. Israelsson, K. Hellström, J.-E. Svensson, L.-G. Johansson, KCl-Induced Corrosion of the FeCrAl Alloy Kanthal ® AF at 600 °C and the Effect of H2O, Oxidation of Metals 83 (2015) 1–27.
[22] N. Israelsson, High temperature oxidation and chlorination of FeCrAl alloys, Chalmers University of Technology, Göteborg, 2014.
[23] L. Mikkelsen, T. Jonsson, M.D. Paz, J. Eklund, J. Liske, B. Jönsson, N. Israelsson, S. Selin, J. Hernblom, J. Högberg, J. Nockert Olovsjö, Increased steam temperature in grate-fired boilers - Steamboost, Energiforsk, 2018.
[24] A. Persdotter, J. Eklund, J. Liske, T. Jonsson, Beyond Breakaway Corrosion - Influence of Chromium, Nickel and Aluminium on Corrosion of Iron-based Alloys at 600 ∘C, Corrosion Science (2020), 108961.
[25] J. Lehmusto, P. Yrjas, B.J. Skrifvars, M. Hupa, High temperature corrosion of superheater steels by KCl and K2CO3 under dry and wet conditions, Fuel Process. Technol. 104 (2012) 253–264.
[26] J. Lehmusto, B.J. Skrifvars, P. Yrjas, M. Hupa, Comparison of potassium chloride and potassium carbonate with respect to their tendency to cause high temperature corrosion of stainless 304L steel, Fuel Process. Technol. 105 (2013) 98–105.
[27] J. Pettersson, J.E. Svensson, L.G. Johansson, Alkali Induced Corrosion of 304-type Austenitic Stainless Steel at 600 degrees C; Comparison between KCl, K2CO3 and K2SO4, in: P. Steinmetz, I.G. Wright, A. Galerie, D. Monceau, S. Mathieu (Eds.), High Temperature Corrosion and Protection of Materials 7, Pts 1 and 2, Trans Tech Publications Ltd, Durnten-Zurich, 2008, pp. 367–375.
[28] J. Sui, J. Lehmusto, M. Bergelin, L. Hupa, Initial oxidation mechanisms of stainless steel Sanicro 28 (35Fe27Cr31Ni) exposed to KCl, NaCl, and K2CO3 under dry and humid conditions at 535 °C, Corrosion Science 155 (2019) 29–45.
[29] B. Pujilaksono, T. Jonsson, H. Heidari, M. Halvarsson, J.-E. Svensson, L.-G. Johansson, Oxidation of binary FeCr alloys (Fe–2.25 Cr, Fe–10Cr, Fe–18Cr and Fe–25Cr) in O 2 and in O 2+ H 2 O environment at 600 C, Oxidation of metals 75 (2011) 183–207.
[30] D.J. Young, High Temperature Oxidation and Corrosion of Metals, Elsevier, 2008.
[31] B. Pujilaksono, T. Jonsson, M. Halvarsson, J.-E. Svensson, L.-G. Johansson, Oxidation of iron at 400–600°C in dry and wet O2, Corrosion Science 52 (2010) 1560–1569.
[32] J. Orman, K. Crispin, Geochemistry, Diffusion in oxides 72 (2010) 757–825.
[33] D. Whittle, G. Wood, D. Evans, D.J.A.M. Scully, Concentration profiles in the underlying alloy during the oxidation of iron-chromium alloys, Acta Metallurgica 15 (1967) 1747–1755.
[34] D. Young, J. Zurek, L. Singheiser, W.J.C.S. Quadakkers, Temperature dependence of oxide scale formation on high-Cr ferritic steels in Ar–H2–H2O, Corrosion Science 53 (2011) 2131–2141.
[35] T. Jonsson, S. Canovic, F. Liu, H. Asteman, J.E. Svensson, L.G. Johansson, M. Halvarsson, Microstructural investigation of the effect of water vapour on the oxidation of alloy 353 MA in oxygen at 700 and 900°C, Materials at High Temperatures 22 (2005) 231–243.
[36] J. Robertson, M.J.M.s. Manning, technology, Healing layer formation in Fe–Cr–Si ferritic steels, Materials Science and Technology 5 (1989) 741–753.
[37] C. Pascal, V. Parry, E. Fedorova, M. Braccini, P. Chemelle, N. Meyer, D. Oquab, D. Monceau, Y. Wouters, M.J.C.S. Mantel, Breakaway oxidation of austenitic stainless steels induced by alloyed sulphur, Corrosion Science 93 (2015) 100–108.
[38] A. Col, V. Parry, C. Pascal, Oxidation of a Fe–18Cr–8Ni austenitic stainless steel at 850°C in O2: Microstructure evolution during breakaway oxidation, Corrosion Science 114 (2017) 17–27.
[39] W.H.J.T.L. Bragg, Edinburgh, D.P. Magazine, J.o. Science, XXX. The structure of the spinel group of crystals, The London, Edinburgh, and Dublin Philosophical Magazine and Journal of Science 30 (1915) 305–315.
[40] X. Liang, Y. Zhong, S. Zhu, H. He, P. Yuan, J. Zhu, Z. Jiang, The valence and site occupancy of substituting metals in magnetite spinel structure Fe3−xMxO4 (M = Cr, Mn, Co and Ni) and their influence on thermal stability: An XANES and TG-DSC investigation, Solid State Sciences 15 (2013) 115–122.
[41] S. Hallström, M. Halvarsson, L. Höglund, T. Jonsson, J. Ågren, High temperature oxidation of chromium: Kinetic modeling and microstructural investigation, Solid State Ionics 240 (2013) 41–50.